Article

Radiation-Induced Paramagnetic Centers in Meso- and Macroporous Synthetic Opals from EPR and ENDOR Data

Alexander Rodionov [1], Larisa Latypova [2,3], Georgy Mamin [1] and Marat Gafurov [1,*]

[1] Institute of Physics, Kazan Federal University, 18 Kremlevskaya Street, 420008 Kazan, Russia
[2] School of Chemistry and Chemical Engineering, Harbin Institute of Technology, 92 West Da-Zhi Street, Harbin 150001, China; larisa.latypova@hit.edu.cn
[3] Zhengzhou Research Institute, Harbin Institute of Technology, 26 Intersection of Longyuan East 7th Street and Longhu Central North Road, Zhengdong New District, Zhengzhou 450046, China
[*] Correspondence: marat.gafurov@kpfu.ru

Abstract: The paramagnetic defects and radiation-induced paramagnetic centers (PCs) in silica opals can play a crucial role in determining the magnetic and electronic behavior of materials and serve as local probes of their electronic structure. Systematic investigations of paramagnetic defects are essential for advancing both theoretical and practical aspects of material science. A series of silica opal samples with different geometrical parameters were synthesized and radiation-induced PCs were investigated by means of the conventional and pulsed X- and W-band electron paramagnetic resonance, and $^1H/^2H$ Mims electron-nuclear double resonance. Two groups of PCs were distinguished based on their spectroscopic parameters, electron relaxation characteristics, temperature and time stability, localization relative to the surface of silica spheres, and their origin. The obtained data demonstrate that stable radiation-induced E' PCs can be used as sensitive probes for the hydrogen-containing fillers of the opal pores, for the development of compact radiation monitoring equipment, and for quantum technologies.

Keywords: opal; pores; paramagnetic centers; EPR; ENDOR

1. Introduction

Synthetic silica opals, with their unique photonic properties and structural characteristics, have garnered significant attention in the fields of materials science and condensed matter physics. These photonic crystals, characterized by their ordered arrangement of silica spheres, exhibit a range of optical phenomena, including iridescence and photonic bandgap effects, which make them promising candidates for various applications such as (photo)catalysis, optics, sensing, energy storage, and telecommunications [1–6]. Paramagnetic centers (PCs), typically arising from defects, impurities, or dopants within the crystal lattice, can play a crucial role in determining the catalytic, magnetic, and electronic behavior of materials. PCs can serve as local probes of the electronic structure, providing insights into the bandgap and conduction mechanisms within the opal matrices [7–11]. Understanding the nature of these defects can lead to the optimization of the material's properties for specific applications, such as enhancing catalytic activity, light–matter interactions, or improving the efficiency of photonic devices.

Interaction between PCs and the surrounding lattice can lead to novel phenomena, such as magneto-optical effects, which have potential applications in (photo)catalysis, spintronics, and quantum computing [1,12,13]. The ability to manipulate and control these interactions opens new avenues for the development of advanced materials with tailored functionalities.

When the materials are subjected to radiation (such as gamma rays, X-rays, etc.) various defects can be created, leading to the formation of stable PCs [14–21]. These centers can serve as valuable probes for understanding the underlying mechanisms of radiation

damage and defect formation, which are critical for the development of radiation-resistant materials. Examining these PCs may result in the creation of novel diagnostic tools for radiation detection and dosimetry [22]. We have demonstrated in earlier research that stable PCs produced by X-rays in porous media made of silica can also yield valuable information about the surface or near-surface state [9], mechanisms of adsorption of polar components of crude oil on silica surface, and heavy oil oxidation processes [10]. Radiation-induced PCs might provide insight into the arrangement of substrates in the porous media and could be used to study catalytic activities [23–25], influence of dimensionality, surface modifications, and size effects [17].

Electron paramagnetic resonance (EPR) is recognized to be an effective method for detecting and quantifying various PCs in a wide range of condensed materials. Although radiation defects in quartz-like materials have been studied by EPR for many decades (see the literature described above and references therein), data on their spectroscopic and time-dependent parameters vary widely. This seems to be due to different methods/conditions of synthesis, storage, treatment, and irradiation of starting materials, as well as to the great diversity of radiation defects observed in the materials under study. The transition to low-dimensional and nanoscale samples, which are necessary for the development of modern technologies, also significantly increases the role of surface effects/defects, which have not yet been fully investigated. High-resolution EPR (in magnetic fields B above 1.5 Tesla), and pulsed EPR techniques which can provide additional information on the behavior of the paramagnetic system and its interaction with its surroundings, have rarely been applied to the study of radiation defects in opals. Data on electronic relaxation times, long values of which are necessary for spin/quantum manipulations, are missing for a number of paramagnetic defects, which does not allow us to compare different systems among themselves to select the most efficient ones. Many experiments in the past were performed only at room and liquid nitrogen temperatures (T = 77 K). The objective of this work was to fill some gaps in the characterization of a number of radiation defects in original synthetic opal samples with EPR.

This paper is devoted to the investigations of radiation-induced PCs in the series of the synthesized opals with different sized silica spheres with conventional and pulsed electron paramagnetic resonance (EPR) and electron-nuclear double resonance (ENDOR) techniques with the aim to attain comprehensive knowledge about the nature of the obtained defects.

2. Materials and Methods

The opal synthesis route was described in detail in Reference [9]. Briefly, ethanol, tetraethylorthosilicate (TEOS, >99.9%), and ammonium hydroxide solution (25% of NH_3) were purchased from Aldrich Inc. (Boston, MA, USA) and utilized without further purification (96%). The two-step-controlled growth method based on the regeneration of silica seeds was used to create silica spheres. The first stage was making the seed dispersion by combining 3.0 mL (40 mmol) of ammonium hydroxide solution, 34 mL (1.9 mole) of deionized water, and 4.5 mL (20 mmol) of TEOS in 80 mL of 100% ethanol. The reaction mixture was kept at 60 °C with stirring for twenty-four hours. Silica nanoparticles of about 20 nm were present in the obtained dispersion. In the second step, 100 mL of the obtained seed dispersion was mixed with 3.75 mL (46 mmol) of ammonium hydroxide solution. Two solutions were then dosed over the course of five hours using a Cole Parmer MasterFlex (Chicago, IL, USA) peristaltic pump: 270 mL of a 1.5 M TEOS solution in ethanol and 270 mL of a 1.2 M NH_3 solution in ethanol. The reaction mixture was kept at 60 °C with stirring for twenty-four hours. The separation of silica particles was achieved using centrifugation at 10,000 rpm, followed by regular washings with ethanol, water-ethanol solutions (1:3, 1:1, and 3:1), and deionized water. After that, the dried silica spheres were calcined for 12 h at 600 °C in a furnace. The desired temperature was reached at a rate of 60° C·h^{-1}.

The isothermal heating evaporation-induced self-assembly (IHEISA) approach was utilized to manufacture silica colloidal crystals by a modified vertical deposition tech-

nique [26]. After using sonication to scatter silica particles in ethanol, a handmade setup was used to maintain 79.8 °C in a glass beaker containing the dispersion. Colloidal crystal fragments were extracted with caution from the beaker walls and then calcined for 12 h at temperatures of 850, 950, and 1000 °C (corresponding to particles with sizes of 93, 274, and 565 nm; these particles are referred to as S, M, and L in this paper).

Scanning electron microscopy (SEM) was used to quantify the particle size in colloidal crystals. SEM observations were performed using a field emission high resolution microscope Merlin (Carl Zeiss, Jena, Germany). Surface morphology observation photos were collected at a 15 kV accelerating voltage for incident electrons and a current of 300 pA.

The ASAP 2020 MP instrument (Micromeritics, Norcross, GA, USA) was used to quantify the surface area of the samples by performing nitrogen adsorption and desorption experiments at 77 K. The Brunauer–Emmett–Teller (BET) equation was utilized to ascertain the specific surface areas of the silica colloid crystal samples. The diameters of the octahedral and tetrahedral pores (d_o, d_t) of the samples were determined to be 0.631 D and 0.368 D, where D is the diameter of the silica sphere [27].

Silica opals are thought to be EPR silent. To create stable radicals in opal, X-ray irradiation of the URS-55 source (U = 55kV, I = 16mA, Wanticathode) at room temperature (RT) for 2 h with the estimated dose of 15 kGy was exploited. To test the influence of the type of irradiation on the observed spectra, the samples were subjected to gamma-irradiation at RT for 90 min ("Microtron-cT", Russia, bremsstrahlung radiation, beam energy 21 MeV, current strength up to 5 μA, pulse repetition time 200 Hz, pulse duration 3 μs, gamma-ray flux 5×10^{13} $(cm^2 \cdot s)^{-1}$, estimated absorbed dose 15–20 kGy). The irradiation was conducted in the A.A. Baikov Institute of Metallurgy and Materials Science (IMET RAS, Moscow). It was found that spectral and relaxation characteristics of the observed PCs do not practically differ from the parameters of the PCs obtained after X-ray irradiation.

EPR investigations were carried out using X-band Bruker ESP 300 (microwave frequency $\nu \approx 9.5$ GHz) and Bruker Elexsys X- and W-band (microwave frequency $\nu \approx 93.5$ GHz) E580/680 spectrometers (all EPR spectrometers were produced in Karlsruhe, Germany) equipped with helium flow cryostats. We used conventional continuous wave (CW) and two-pulse field swept electron spin echo (FS ESE) measurements for the detection of EPR signal and the primary Hahn-echo ($\pi/2$-τ-π-echo), where τ is the interpulse delay time of 240 ns, with the $\pi/2$ and π pulse lengths of 40 and 80 ns for the X-band, and 32 and 64 ns for the W-band, respectively. For measurements of the spin-lattice relaxation times (T_{1e}), the inversion-recovery sequence with an additional inverting π-pulse (π-$\pi/2$-τ-π-echo) was used. For the W-band ENDOR experiments special cavities and Mims pulse sequence ($\pi/2$-τ-$\pi/2$-T-$\pi/2$) with an additional radiofrequency (RF) pulse $\pi_{RF} = 18$μs inserted between the second and third microwave $\pi/2$ pulses were exploited. The RF in our setup could be swept into the range of 1–200 MHz. Details of the EPR, ENDOR pulsed measurements, and determination of the electron relaxation parameters are given in paper [28]. The EPR and ENDOR spectra were fitted by exploiting the Easyspin program (version 5.1.0) for Matlab [29].

Protonated (DMSO-H6) and deuterated (DMSO-D6) dimethyl sulfoxide (DMSO) to fill the opal pores for the investigation of electron–nuclear interactions was purchased from Aldrich.

3. Results and Discussion

Figure 1 and Table 1 present the data of the geometric characterization of the synthesized materials. As it was already mentioned in Section 2, three series of opal samples (S, M, and L) with the average sizes of the silica spheres of 93, 274, and 565 nm were distinguished and investigated by EPR techniques.
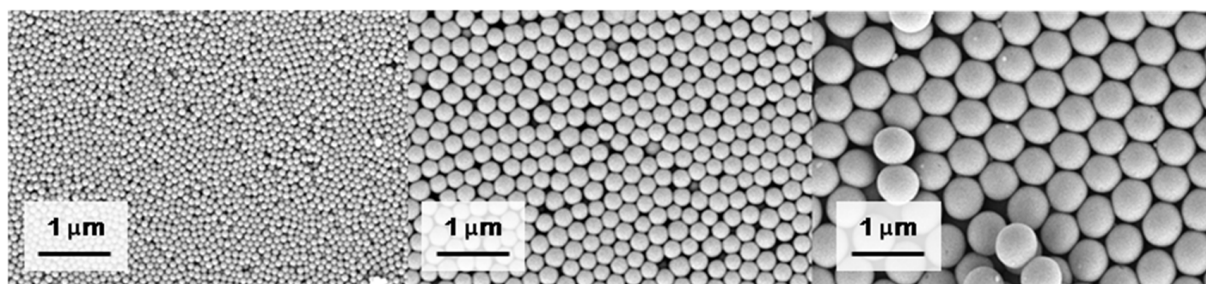
Figure 1. SEM images of synthesized opal samples (from left to right: S, M, L).

Table 1. Average size of silica spheres, BET surface area (a_s(BET)), pore volume, porosity (Φ), and calculated octahedral (d_o) and tetrahedral (d_t) pores diameters (spherical pore model) for synthesized samples.

Sample	Average Size, nm	a_s(BET), m^2 g^{-1}	Pore Volume, cm^3 g^{-1}	Φ	d_o, nm	d_t, nm
S	93 ± 6	33.8 ± 0.2	0.23 ± 0.01	0.33 ± 0.01	59	34
M	274 ± 15	9.4 ± 0.1	0.19 ± 0.01	0.28 ± 0.01	173	101
L	565 ± 20	5.1 ± 0.1	0.22 ± 0.01	0.32 ± 0.01	357	208

The data are presented in Table 1.

No EPR signal was registered for the initial, non-irradiated samples within the sensitivity limits of our equipment, evidencing the absence of paramagnetic impurities and secondary paramagnetic phases. After the irradiation of the samples, the EPR spectra were observed (see Figures 2–5). Their spectra are close to each other for samples S, M, and L and represent a superposition of absorption lines in the region of spectroscopic g-factor 2. Examples of the X-band spectra for the S sample at two microwave power levels are shown in Figure 2a. For a better signal-to-noise ratio, the temperature was lowered; however, conventional EPR can also be observed at ambient conditions and at RT. The arrows point out the features of the observed EPR spectra with the corresponding spectroscopic g-factors.

Four main types of EPR lines in silica are considered in the literature.

Type 1. One main type is the EPR line with g = 2.006. It is characteristic of the EPR lines of broken silicon bonds in crystalline and amorphous Si and in amorphous SiO_2 layers, in which the g-factor varies from 2.006 to 2.0006. The determined value of g is closer to the value of 2.006 and indicates that these defects are due to defects in the SiO_2 phase and can be depicted as $SiOO\cdot$ or $SiO_2\equiv Si–$ [15].

Type 2. Other lines of spectra are usually attributed to peroxy radicals (POR) [30]. The POR is a molecular ion O_2^- bonded to one Si atom in the SiO_2 matrix, i.e., it has the configuration $O_3\equiv Si–O–O\cdot$. For POR in SiO_2, the literature provides the following values of the g-tensor components defined by the orthorhombic symmetry of the complex: $g_1 = 2.0019 \pm 0.0002$; $g_2 = 2.0072 \pm 0.0002$; $g_3 = 2.067 \pm 0.003$ [31].

Type 3. The third type focuses on the defects associated with broken bonds of oxygen atoms, the non-bridging oxygen hole center (NBOHC, $O_3\equiv Si–O\cdot$). For NBOHC, the literature data provide $g_1 = 2.0100$ and $g_2 = 2.0010$ [31,32]. In our experiments, we did not observe these lines.

Type 4. A line from the E'-center that easily saturates with microwave power and this helps to distinguish it from the mentioned above three types of lines (Figure 2c). We determined for the E'-center spin-lattice (longitudinal) relaxation times $T_1 \approx 1$ μs at T = 300 K in the X-band and $T_1 \approx 700$ μs in the W-band at T = 120 K (Figure 2b) (at RT in the W-band the electron relaxation times were too short to measure). It was found that T_1 does not depend on the average size of the silica sphere.
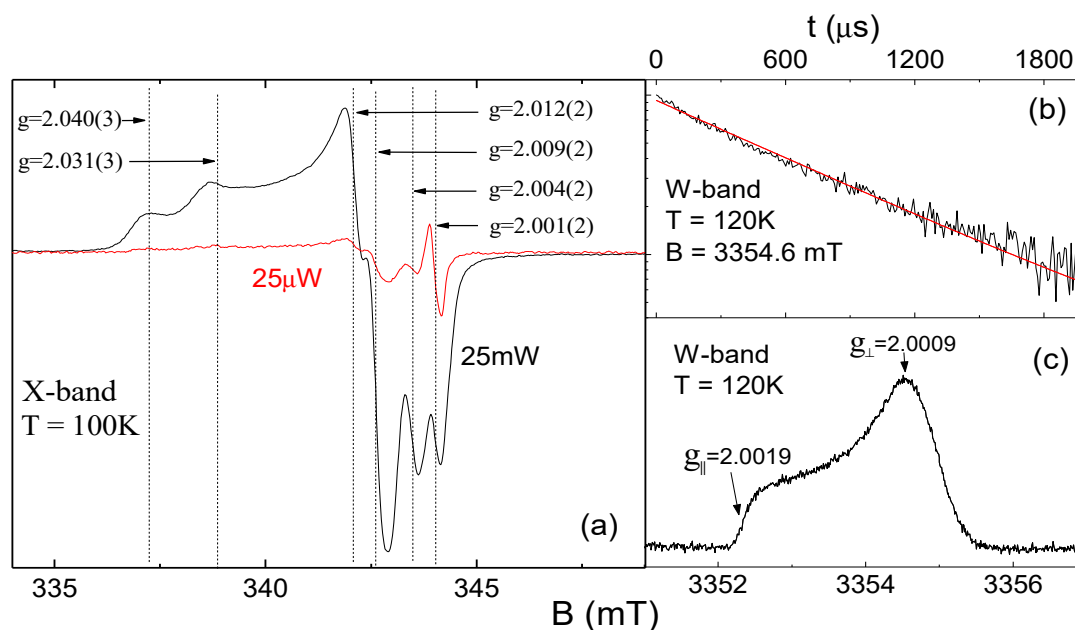
Figure 2. (**a**) The X-band CW EPR spectrum for S sample acquired at T = 100 K and the different values of the microwave power (25 mW—red line and 25 µW—black line) immediately after X-ray irradiation. The arrows indicate the features of the spectrum and the values of g-factors for them. (**b**) The inversion-recovery curve multiplied by (−1) for sample S at T = 120 K in the W-band in the magnetic field corresponding to $g_\perp$ = 2.0009 (black curve), and its approximation with the monoexponential function with T1 = 711 ± 50 µs (red line). (**c**) The W-band pulsed EPR spectrum for S sample at T = 120 K; the features of the spectrum of axial symmetry with $g_\parallel$ = 2.0019, and $g_\perp$ = 2.0009 are marked.
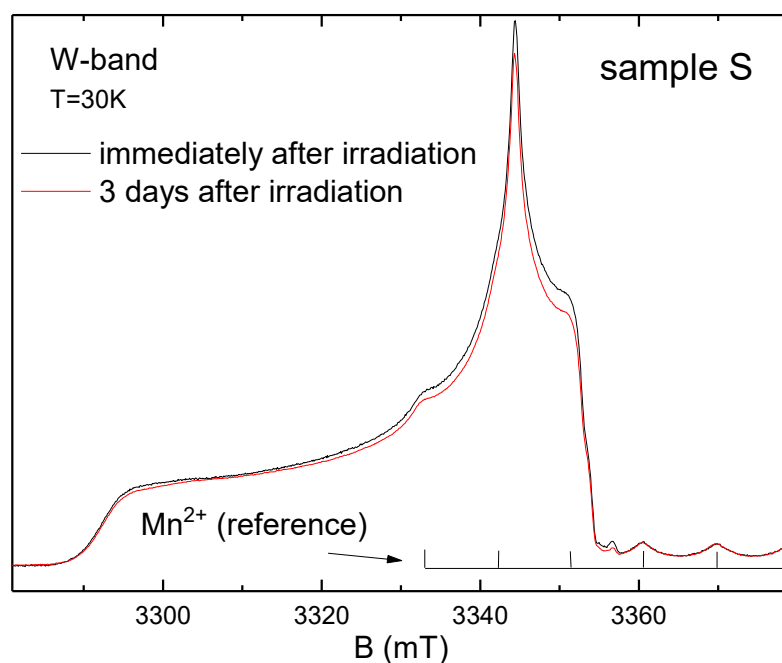

Figure 3. The W-band EPR spectrum of S sample at T = 30 K immediately after X-ray irradiation (black curve), and 3 days after irradiation (red curve). The arrows indicate the changing of the spectrum due to PCs recombination. The grid of six lines marks the hyperfine structure of Mn^{2+} ion in the reference sample.
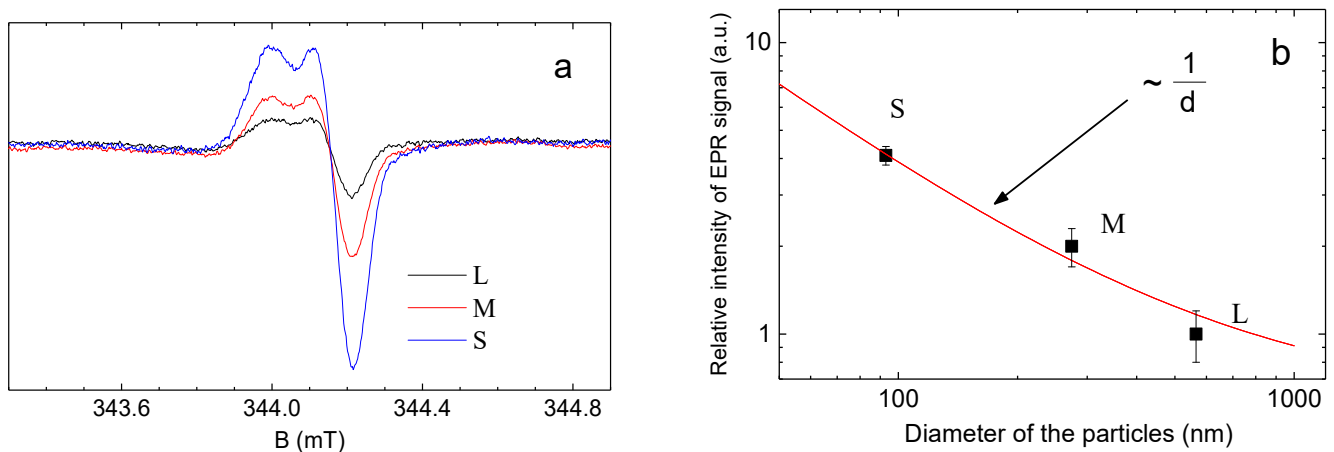
Figure 4. (**a**) The X-band CW EPR of the X-ray irradiated samples for L (black line), M (red line), and S (blue line) detected at T = 100 K in the same experimental conditions. The value of the microwave power is 25 µW. The intensities (amplitudes) of the spectra are normalized to the masses of the samples. (**b**) The dependence of the relative EPR intensity of E'-centers on the characteristic size of particles in the log–log scale. The red line is the approximation by the function f(x) = A/d, where d is the diameter of the particles and A is a fitting coefficient.
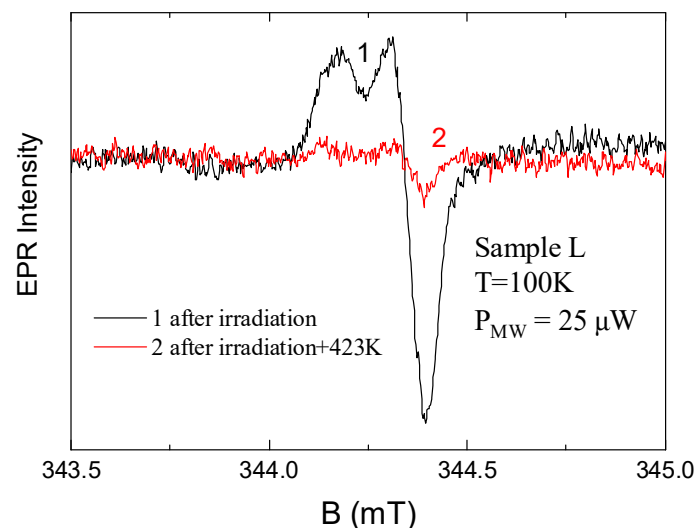

Figure 5. The X-band CW EPR spectrum for sample L at T = 100 K acquired in the same experimental conditions before annealing (black curve 1), and after annealing at T = 423 K for 10 min (red curve 2).

The obtained spectroscopic parameters are typical for E'-centers, which are broken Si bonds in SiO_2 with the $O_3{\equiv}Si$-configuration (E defects are usually subdivided into E' and E'' to indicate the presence of one and two trapped electrons, respectively). X- and W-band measurements provide the following spectral parameters for the PC of axial symmetry: $g_{\parallel}$ = 2.0019 ± 0.0005 and $g_{\perp}$ = 2.0009 ± 0.0005 [9]. It was found that spectroscopic parameters of the E'-centers do not depend on the size of the silica spheres (see Figures 2c, 4a and 5).

The other three types of EPR signals are not saturated (do not disappear) with high microwave power. Figure 3 shows the W-band pulsed EPR spectra acquired for the freshly irradiated sample S, and also for the same sample 3 days after irradiation. To exclude the signal from the easily microwave-power-saturated E'-center, measurements were performed at the maximum achievable microwave power (about 100 mW) at T = 30 K. The noticeable change in spectrum occurs due to the paramagnetic centers recombination

in the range of g = 2.016–2.006. Therefore, it can be assumed that lines with such a g–factor range belong to the type of paramagnetic centers that decay slightly faster than the others.

The spectrum of the E′ center is stable and almost completely disappears after annealing for 10 min at T = 423 K (Figure 5). The time decay of the EPR intensity of the induced E′-centers at RT after X-ray irradiation measured at the X-band is shown in Figure 6. For all of the studied samples, the decay curves are the same and can be approximated by one exponent, which indicates the similar nature and type of investigated EPR centers in all samples. The half-life period was estimated as $t_{1/2}$ = 648 ± 30 h from the following equation [33]:

$$t_{1/2} = t \cdot \ln(2)/\ln(N_0/N_t), \tag{1}$$

where t is the elapsed time, N_0 is the initial amount of PCs of the substance, and N_t is the amount of PCs after time t.
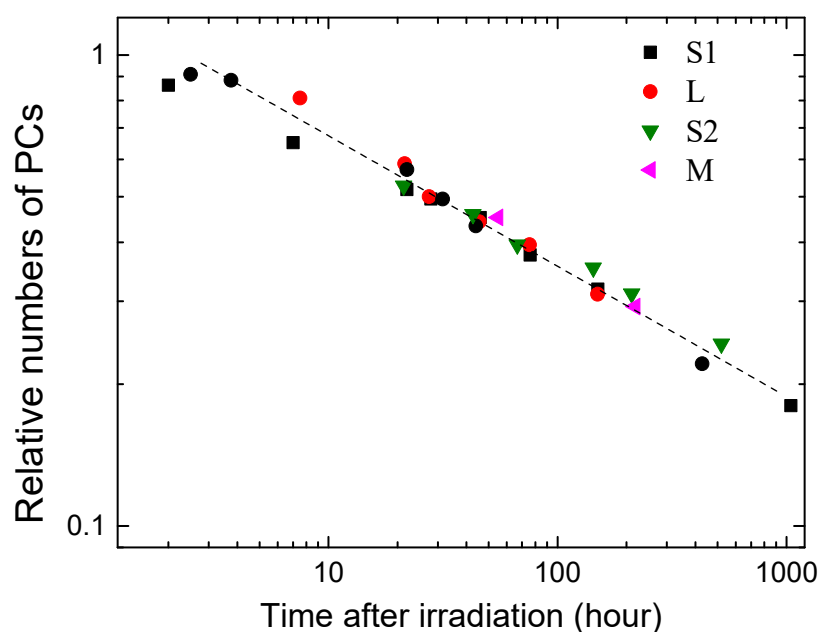

Figure 6. Decay curve of EPR intensity of induced E′-centers in log–log scale. S1 and S2 are S samples synthesized one week apart.

The dependence of the EPR line intensity of the E′-centers on the characteristic sizes of SiO_2 particles is presented in Figure 4. Since the intensity of the EPR lines is proportional to the concentration of PCs, and the irradiation dose in all samples is the same, we can compare the concentrations of the induced paramagnetic centers in SiO_2 particles of different sizes. Figure 4b shows the inverse dependence of the intensity with the particle size: when the characteristic particle size decreases, the concentration of paramagnetic centers increases. Such inverse dependence (taking into account the results of the ENDOR experiments presented below and the fact that the pore volumes are roughly the same for all the samples, see Table 1) may serve as evidence that the E′-centers are not bulk PCs (are not located in the volume) and are not distributed on the SiO_2 surface but in the near surface layer of the SiO_2 spheres (in the shell of the core–shell model, see [34]). In Reference [34], the concentration of the nitrogen and nitrogen-vacancy centers in (nano)diamonds was investigated and the locations of PCs of different origins were established from the analysis of the EPR intensity with particle size. Since we examined only three samples in our experiments, the exact functional relation and estimates of the surface layer thickness in which E′-centers are distributed are not given here.

The SiO_2 pores were filled with solutions of protonated and deuterated DMSO in order to investigate the localization of the induced paramagnetic centers and the extent of their reactivity. For the experiment, sample M was selected. Two scenarios were examined:

in the first, DMSO was first used to fill (infiltrate) the pores of the samples, and then X-ray irradiation was performed; in the second scenario, the sequence of events was switched. Two types of DMSO molecules were used in the investigation of the nature of the bonds that were formed between the induced paramagnetic centers and the molecules: protonated (DMSO-H6) and deuterated (DMSO-D6). As a result, four different types of spectra were examined for both qualitative and quantitative change assessment (Figure 7).
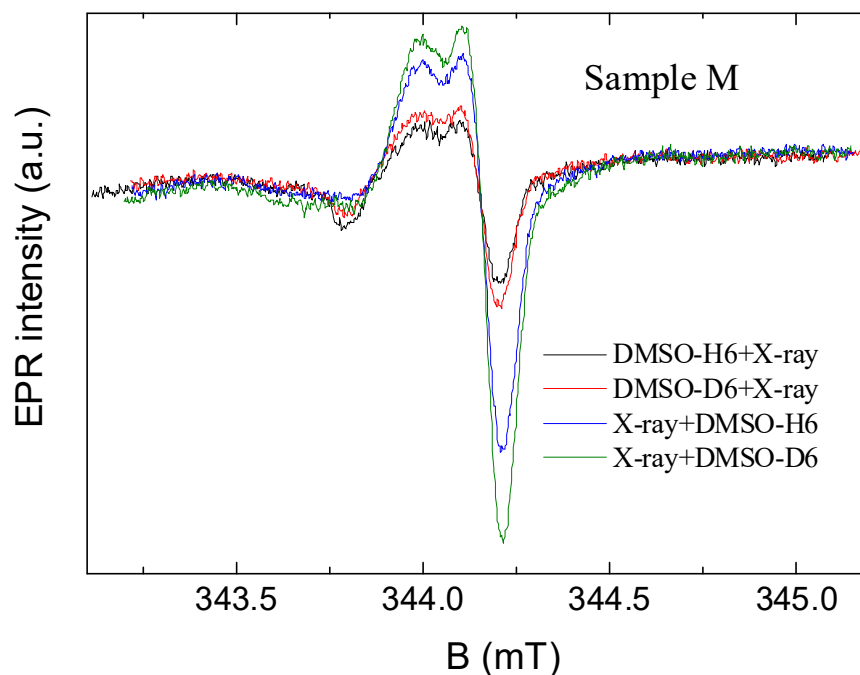

Figure 7. EPR spectra of induced E'-centers acquired at T = 100 K at different orders of irradiation and filling of M sample.

Consequently, it can be observed that while the parameters of the E'-center spectrum in each of the four cases under investigation do not change, the intensity of the spectra in the case where the samples were irradiated prior to being filled with DMSO is noticeably higher than in the case of the opposite order of actions. Presumably, the presence of DMSO molecules in the adsorbed near-surface layer prevents some of the PCs from forming on the surface of SiO_2 particles after X-ray irradiation.

Even though the infiltrated samples' EPR spectra have the same parameters as the non-infiltrated samples, their spectra cannot be detected at RT because infiltration causes the EPR signals' intensity to sharply decrease and the E'-centers' relaxation times to shorten. Contrastingly, in the original opals, the T_1 is about 1 μs at T = 300 K in the X-band and about 700 μs in the W-band at T = 120 K, for the infiltrated samples the value T_{1e} of 1 μs was reached only at T ≈ 15 K for both frequency ranges.

While the spectral and relaxation characteristics of the radiation PCs do not change upon introduction of ^1H or ^2H DMSO (Figure 7), different W-band ENDOR spectra of the interaction of proton and deuterium nuclei with PCs in opal were recorded. We were not able to detect either ^1H or ^2H ENDOR spectra for the first and second types of PCs. This most likely indicates a "deeper" embedding of these PCs in the SiO_2 thickness and/or their well localized electron density function, which does not allow detection of weak electron–nuclear interactions with solvent nuclei. Thus, PCs of types 1 and 2 can hardly be used to analyze reaction processes in opal pores.

Well-resolved ^1H-ENDOR splittings were obtained for both values of the external magnetic field corresponding to the $g_\parallel$ and $g\perp$ (see Figure 2c). The ^1H-ENDOR spectra for the E' center detected at T = 100 K in the magnetic fields corresponding to the $g_\perp$ = 2.0009 are presented in Figure 8.
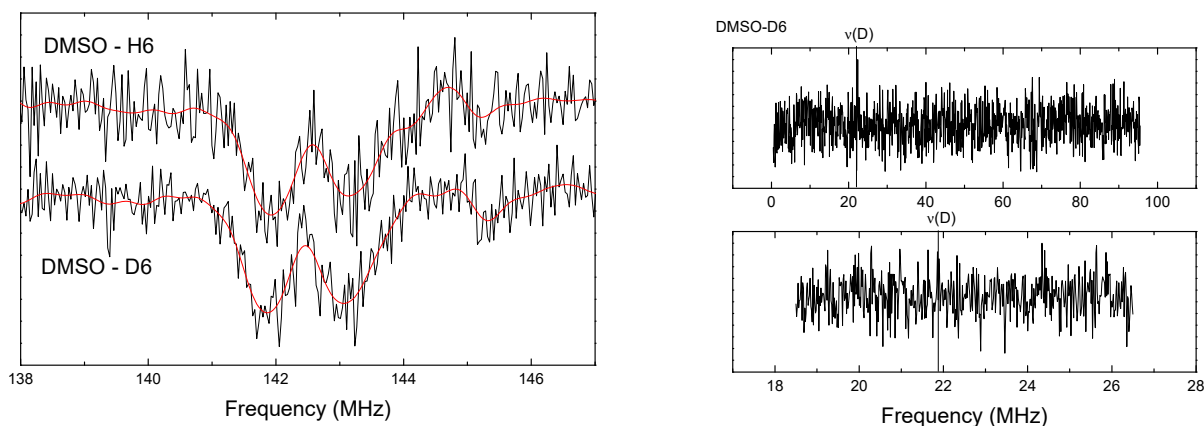
Figure 8. (**a**) [1]H-ENDOR (W-band) for opals filled with DMSO-H6 and DMSO-D6 at T = 100 K in magnetic fields corresponding to $g_\perp$ of E'-center. Red lines are Easyspin fittings by using Equation (2) with electron-proton distance *r* = 0.41 nm; (**b**) [2]H-ENDOR (W-band) for opals filled with DMSO-D6 at T = 50 K in magnetic fields corresponding to $g_\parallel$ (upper panel) and $g\perp$ (lower panel) components of E'-center.

The [1]H-ENDOR patterns and ratio between the splittings for two orientations (roughly 2:1) allows us to make an assumption that the strong electron–proton hyperfine interaction originates mainly from the dipolar interaction. In the approximation of electron–proton point-dipole interaction between electron and nuclear spins, one can observe the RF splitting depending on the electron-proton distance r as follows:

$$\left|\Delta f\right| = g_S g_I \beta_S \beta_I (3\cos^2\Theta - 1)/r^3, \tag{2}$$

where g_S, g_I, β_S, β_I are the *g*-factors and Bohr's magnetons of the electron and nucleus, respectively, and Θ is the polar angle between the direction of the applied magnetic field and the line connecting the *S* and *I* spins [9]. The obtained value of Δf corresponds to electron-proton distance of 0.41 nm. It shows that stable E' centers are localized near the silica sphere surface.

No splitting was observed in the [2]H-ENDOR experiments with the deuterated DMSO solution (Figure 8b). The ENDOR spectra for ^{2}H by exploiting the deuterated DMSO shows itself as a line on the Larmor frequency of ^{2}H due to the interaction with the remote nuclei (r > 10 nm). The obtained data testify in favor of the formation of stable bonds (complexes) of hydrogen with surface PCs.

The obtained data demonstrate that stable radiation-induced E'paramagnetic centers could be used as sensitive probes for the hydrogen-containing fillers of the opal pores.

4. Conclusions

The main results of the work can be summarized as follows:

1. After X-ray and gamma-irradiation at RT in all samples, two groups of paramagnetic centers (unstable and fast relaxing vs. more stable and slower relaxing E'-centers) are formed. The first group is ascribed to the presence of two types of PCs, namely to the broken silicon bonds in SiO_2 ($SiOO\cdot$ or $SiO_2\equiv Si–$), and peroxy radicals $O_3\equiv Si–O–O\cdot$.

2. By using pulsed high-field W-band EPR, the spectroscopic parameters g_1 = 2.0020 ± 0.0004; g_2 = 2.0060 ± 0.0002; and g_3 = 2.0372 ± 0.002, which are not dependent on the average size of the silica spheres for the peroxy radicals, were defined with high precision.

3. For the long relaxing E'-centers ($T_1 \approx 1$ μs at T = 300 K in the magnetic field of 340 mT and $T_1 \approx 700$μs at T = 120 K in the magnetic field of 3400 mT), the intensity of the EPR spectra inversely depends on the average size of the silica spheres. It is ascribed to

the preferable location of the E'-centers in the shell (in the near surface layer) of the SiO_2 spheres.

4. The half-life of the EPR intensity time decay at room temperature was defined as $t_{1/2} = 648 \pm 30$ h and does not depend on the average size of the silica spheres. The EPR spectra disappear (within the sensitivity of our equipment) after annealing for 10 min at $T = 423$ K. The sensitivity of the EPR spectrum intensity to irradiation, the size of silica spheres, and the possibility of the rapid annealing of radiation-induced paramagnetic centers make the considered system suitable for the development of compact radiation monitoring equipment.

5. From the W-band ENDOR experiments with filling pores with DMSO, it follows that E'-centers can be used for proton sensing. The ENDOR experiments also confirm that the E'-centers obtained by EPR are mainly distributed in the near-surface layer of the silica spheres. Stability, relative narrow EPR spectrum, long relaxation times even in the high magnetic fields of 3400 mT, and strong electron–nuclear interaction with protons of DMSO allow us to consider E'-centers in opal as a model of the two-dimensional system for the development of quantum technologies.

References

1. Singh, B.; Na, J.; Konarova, M.; Wakihara, T.; Yamauchi, Y.; Salomon, C.; Gawande, M.B. Functional mesoporous silica nanomaterials for catalysis and environmental applications. *Bull. Chem. Soc. Jpn.* **2020**, *93*, 1459–1496. [CrossRef]
2. Joannopoulos, J.D.; Johnson, S.G.; Winn, J.N.; Meade, R.D. *Photonic Crystals: Molding the Flow of Light*, 3rd ed.; Princeton University Press: Princeton, NJ, USA, 2008; pp. 1–304.
3. Marlow, F.; Muldarisnur Sharifi, P.; Brinkmann, R.; Mendive, C. Opals: Status and prospects. *Angew. Chem. Int. Ed.* **2009**, *48*, 6212–6233. [CrossRef] [PubMed]
4. Armstrong, E.; O'Dwyer, C. Artificial opal photonic crystals and inverse opal structures–fundamentals and applications from optics to energy storage. *J. Mater. Chem. C* **2015**, *3*, 6109–6143. [CrossRef]
5. Fathi, F.; Rashidi, M.R.; Pakchin, P.S.; Ahmadi-Kandjani, S.; Nikniazi, A. Photonic crystal based biosensors: Emerging inverse opals for biomarker detection. *Talanta* **2021**, *221*, 121615. [CrossRef] [PubMed]
6. Olla, C.; Carbonaro, C.M. The void side of silica: Surveying optical properties and applications of mesoporous silica. *J. Phys. Condens. Matter* **2024**, *36*, 253002. [CrossRef]
7. D'Arienzo, M.; Morazzoni, F.; Ruffo, R.; Scotti, R. Using the electron spin resonance to detect the functional centers in materials for sensor devices. *Ionics* **2021**, *27*, 1839–1851. [CrossRef]
8. Salh, R. Defect related luminescence in silicon dioxide network: A review. In *Crystalline Silicon-Properties and Uses*; Basu, S., Ed.; InTechOpen: Rijeka, Croatia, 2011; pp. 135–172. [CrossRef]
9. Galukhin, A.; Osin, Y.; Rodionov, A.; Mamin, G.; Gafurov, M.; Orlinskii, S. Radiation-induced paramagnetic centers in nanoporous synthetic opals–a probe for near surface protons. *Magn. Reson. Solids* **2018**, *20*, 18203.
10. Gafurov, M.; Galukhin, A.; Osin, Y.; Murzakhanov, F.; Gracheva, I.; Mamin, G.; Orlinskii, S. Probing the surface of synthetic opals with the vanadyl containing crude oil by using EPR and ENDOR techniques. *Magn. Reson. Solids* **2019**, *21*, 19101. [CrossRef]

11. Kühnhold-Pospischil, S.; Saint-Cast, P.; Hofmann, M.; Weber, S.; Jakes, P.; Eichel, R.A.; Granwehr, J. A study on Si/Al_2O_3 paramagnetic point defects. *J. Appl. Phys.* **2016**, *120*, 195304. [CrossRef]

12. Jansen, R. Silicon spintronics. *Nat. Mater.* **2012**, *11*, 400–408. [CrossRef]

13. Arora, A. Magneto-optics of layered two-dimensional semiconductors and heterostructures: Progress and prospects. *J. Appl. Phys.* **2021**, *129*, 120902. [CrossRef]

14. Griscom, D.L. Trapped-electron centers in pure and doped glassy silica: A review and synthesis. *J. Non-Cryst. Solids* **2011**, *357*, 1945–1962. [CrossRef]

15. Alessi, A.; Agnello, S.; Buscarino, G.; Pan, Y.; Mashkovtsev, R.I. EPR on Radiation-Induced Defects in SiO_2. In *Applications of EPR in Radiation Research*; Lund, A., Shiotani, M., Eds.; Springer: Berlin/Heidelberg, Germany, 2014; pp. 255–295. [CrossRef]

16. Alessi, A.; Agnello, S.; Buscarino, G.; Boizot, B.; Cannas, M.; Gelardi, F.M. β-ray irradiation effects on silica nanoparticles. *IOP Conf. Ser. Mater. Sci. Eng.* **2015**, *80*, 012011. [CrossRef]

17. Murphy, D.M.; Chiesa, M. EPR of paramagnetic centres on solid surfaces. In *Electron Paramagnetic Resonance, Volume 21*; Gilbert, B.C., Ed.; RSC Publishing: London, UK, 2008; pp. 105–130. [CrossRef]

18. Gromov, O.I.; Feklichev, E.D.; Zhidomirov, G.M.; Rybaltovskii, A.O.; Sviridov, A.P.; Grigoriev, Y.V.; Ischenko, A.A.; Bagratashvili, V.N.; Golubeva, E.N. Influence of solvent electron affinity on paramagnetic defects in hybrid Si/SiOx luminescent nanoparticles. *J. Nanopart. Res.* **2019**, *21*, 127. [CrossRef]

19. Agnello, S.; Boscaino, R.; Cannas, M.; Gelardi, F.M. Creation of paramagnetic defects by gamma irradiation in amorphous silica. *Appl. Magn. Reson.* **2000**, *19*, 579–585. [CrossRef]

20. Mahmud, H.H.; Mansour, A.; Ezz-Eldin, F.M. Generation and bleaching of E′-centers induced in a-SiO_2 by γ-irradiation. *J. Radioanal. Nucl. Chem.* **2014**, *302*, 261–272. [CrossRef]

21. Stesmans, A.; Clémer, K.; Afanas'ev, V.V. Electron spin resonance probing of fundamental point defects in nanometer-sized silica particles. *Phys. Rev. B* **2005**, *72*, 155335. [CrossRef]

22. Aboelezz, E.; Pogue, B.W. Review of nanomaterial advances for ionizing radiation dosimetry. *Appl. Phys. Rev.* **2023**, *10*, 021312. [CrossRef]

23. Bracci, M.; Bruzzese, P.C.; Famulari, A.; Fioco, D.; Guidetti, A.; Liao, Y.K.; Podvorica, L.; Rezayi, S.F.; Serra, I.; Thangavel, K.; et al. Paramagnetic species in catalysis research: A unified approach towards (the role of EPR in) heterogeneous, homogeneous and enzyme catalysis. In *Electron Paramagnetic Resonance: Volume 27*; Chechik, V., Murphy, D.M., Bode., B.E., Eds.; RCS: Croydon, UK, 2020; pp. 1–46. [CrossRef]

24. Goldberg, M.A.; Akopyan, A.V.; Gafurov, M.R.; Makshakova, O.N.; Donskaya, N.O.; Fomin, A.S.; Polikarpova, P.P.; Anisimov, A.V.; Murzakhanov, F.F.; Leonov, A.V.; et al. Iron-doped mesoporous powders of hydroxyapatite as molybdenum-impregnated catalysts for deep oxidative desulfurization of model fuel: Synthesis and experimental and theoretical studies. *J. Phys. Chem. C* **2021**, *125*, 11604–11619. [CrossRef]

25. Alessi, A.; Kuhnhenn, J.; Buscarino, G.; Di Francesca, D.; Agnello, S. The relevance of point defects in studying silica-based materials from bulk to nanosystems. *Electronics* **2019**, *8*, 1378. [CrossRef]

26. Wong, S.; Kitaev, V.; Ozin, G.A. Colloidal Crystal Films: Advances in Universality and Perfection. *J. Am. Chem. Soc.* **2003**, *125*, 15589–15598. [CrossRef]

27. Galukhin, A.; Bolmatenkov, D.; Emelianova, A.; Zharov, I.; Gor, G.Y. Porous Structure of Silica Colloidal Crystals. *Langmuir* **2019**, *35*, 2230–2235. [CrossRef] [PubMed]

28. Latypova, L.R.; Mukhamatdinov, I.I.; Rodionov, A.A.; Shurtakova, D.V.; Gafurov, M.R. Temperature Dependence of the Electron Spin–Lattice Relaxation Time of Vanadyl Porphyrins in Asphaltenes from the Ashalcha Oilfield. *Appl. Magn. Reson.* **2024**, *55*, 1221–1232. [CrossRef]

29. Stoll, S.; Schweiger, A. EasySpin, a comprehensive software package for spectral simulation and analysis in EPR. *J. Magn. Reson.* **2006**, *178*, 42–55. [CrossRef] [PubMed]

30. Stapelbroek, M.; Griscom, D.L.; Friebele, E.J.; Sigel, G.H., Jr. Oxygen-associated trapped-hole centers in high-purity fused silicas. *J. Non-Cryst. Sol.* **1979**, *32*, 313–326. [CrossRef]

31. Griscom, D.L.; Brinker, C.J. Influence of Processing Parameters on the Defect Structures of Gel-Derived Silicas. *Defect Diffus. Forum* **1987**, *53–54*, 213–226. [CrossRef]

32. Griscom, D.L.; Friebele, E.J. Fundamental defect centers in glass: Si 29 hyperfine structure of the nonbridging oxygen hole center and the peroxy radical in a-SiO_2. *Phys. Rev. B* **1981**, *24*, 4896. [CrossRef]

33. Shukla, A.K. ESR Applications in Paleontology and Geochronology. In *ESR Spectroscopy for Life Science Applications: An Introduction—Techniques in Life Science and Biomedicine for the Non-Expert*; Springer: Cham, Switzerland, 2021. [CrossRef]

34. Yavkin, B.V.; Mamin, G.V.; Gafurov, M.R.; Orlinskii, S.B. Size-dependent concentration of N0 paramagnetic centres in HPHT nanodiamonds. *Magn. Reson. Solids* **2015**, *17*, 15101.